

## **Investigation of the Weld Properties of Inconel 625 based on Nb Content**

*Jeong Won Han<sup>1</sup>, Sang Hoon Jung<sup>2</sup>, Hyunhak Cho<sup>2</sup>, Hae Woo Lee<sup>1,\*</sup>*

<sup>1</sup> Department of Metallurgical Engineering, Dong-A University, Busan Rep. of Korea

<sup>2</sup> R&D Institute, Chosun Welding Co. Ltd., Ulsan Rep. of Korea

\*E-mail: [hwlee@dau.ac.kr](mailto:hwlee@dau.ac.kr)

*Received: 20 July 2017 / Accepted: 6 December 2017 / Published: 5 February 2018*

---

In this study, shielded metal arc welding was performed on Inconel 625 as a function of Nb content at 2.24 wt%, 3.25 wt%, and 4.26 wt%. The microstructure was observed using scanning electron microscopy/energy dispersive X-ray spectroscopy(SEM/EDS) and showed the development of a columnar dendrite structure in the specimen having the least Nb content. From the hardness test, the hardness value was confirmed to reduce with decreasing Nb content. From electron backscatter diffraction(EBSD) analysis, the largest grain size was found in the specimen with Nb content of 2.24 wt%. The potentiodynamic polarization test was carried out to determine the pitting corrosion resistance; there was no significant difference in the pitting corrosion resistance with increasing Nb content. To evaluate the degree of sensitization for intergranular corrosion, the Double Loop Electrochemical Potentiodynamic Reactivation(DL-EPR test) was conducted. A similar degree of sensitization was found in two specimens except with a Nb content of 2.24 wt%, while a relatively high degree of sensitization was found in the specimen with a Nb content of 2.24 wt%.

---

**Keywords:** Inconel 625, Nb content, potentiodynamic test, DL-EPR test

### **1. INTRODUCTION**

In the twentieth century, there has been increasing interest in high-technology industries such as the aerospace industry, nuclear industry, power plant industry, and the petrochemical industry. In particular, an increase in oil price leads to a dramatic increase in new energy fields such as petrochemical plants, power generators, crude oil and gas mining, and drill ships. Since the crude oil or gas extracted from the bottom of the sea is in a strongly corroding environment containing Chlorides, H<sub>2</sub>S, and CO<sub>2</sub>, exploitation requires a highly corrosion resistant alloy in the structure [1-5]. In addition, the corrosion resistant material is essential for preventing structural damage due to corrosion since it is

impossible to repair and maintain the original properties of the offshore platform after installation. The duplex stainless steel employed in existing plants is a highly corrosion resistant material. Nevertheless, a secondary phase is formed when heat is applied, causing brittleness and corrosion [27,28]. As an alternative material to solve this problem, Inconel alloys are in the spotlight. Inconel alloys are Ni-based super heat resistant alloys with Ni-Cr-Mo as the main alloying elements. They have been used as structural materials for steam generators in nuclear reactors and aircraft engines owing to their excellent mechanical properties at high temperature and high corrosion resistance in various corrosive environments [6-11]. In particular, Inconel625 has been reported to prevent rapid age hardening after welding due to the lower Ti and Al amounts and the higher Nb amount compared to other Inconel alloys. Moreover, it can prevent weld cracking by chromium carbide precipitation at grain boundaries [26]. The Inconel alloy with low Nb content has the disadvantages of rapid age hardening after welding and chromium-carbide( $M_{23}C_6$ ) formation at grain boundaries. Inconel 625 is characterized by the precipitation and hardening of a  $\gamma''$  phase in the form of  $Ni_3Nb$ , resulting in excellent oxidation resistance, creep resistance, and high strength at high temperature. In the case of Inconel alloy, carbides and intermetallic compounds ( $\mu$ ,  $\sigma$ , and Laves) are formed during the solidification process after welding, inhibiting workability at high temperature. Particularly, the range of solidification temperatures is expanded in Inconel 625 containing Nb since a secondary phase is formed in the final solidification stage after Nb, Si, and C precipitation. In other words, a eutectic liquid film with low melting point is formed at the dendritic boundary in the final stage of solidification. When stress is applied to the low melting point liquid film ( $\gamma$ /Laves), cracks are generated [26]. As a result, the changes in Nb, Si, and C components affect the range of solidification temperature and the amount and shape of the eutectic phase, determining the solidification cracking susceptibility. The increasing amount of these three components may also deteriorate weldability. Thus, the determination of the proper Nb content that can prevent corrosion at grain boundaries without the deterioration of weldability due to solidification cracking in Inconel625 alloy is essential [15]. In this study, Shielded Metal Arc Welding(SMAW) was performed using three kinds of Inconel 625 Filler metal with different Nb contents. Three kinds of specimen with different Nb contents were fabricated and the effect of the Nb content on microstructure and corrosion behavior of the Inconel625 weld was investigated.

## 2. EXPERIMENTAL METHODS

### 2.1. Specimen fabrication

Three specimens with different Nb contents were prepared by the SMAW technique after two-layer buttering on carbon steel of grade ASTM A36 SS400. The shapes of the welds are illustrated in Fig. 1 and the welding conditions for the three specimens are presented in Table 1. Table 2 shows the weld compositions of the three specimens with different Nb contents. The composition was determined using spark emission spectrometer. For convenience, the specimens with Nb contents of 2.24 wt%, 3.25 wt%, and 4.26 wt% were labeled as No.1, No.2, and No. 3, respectively.

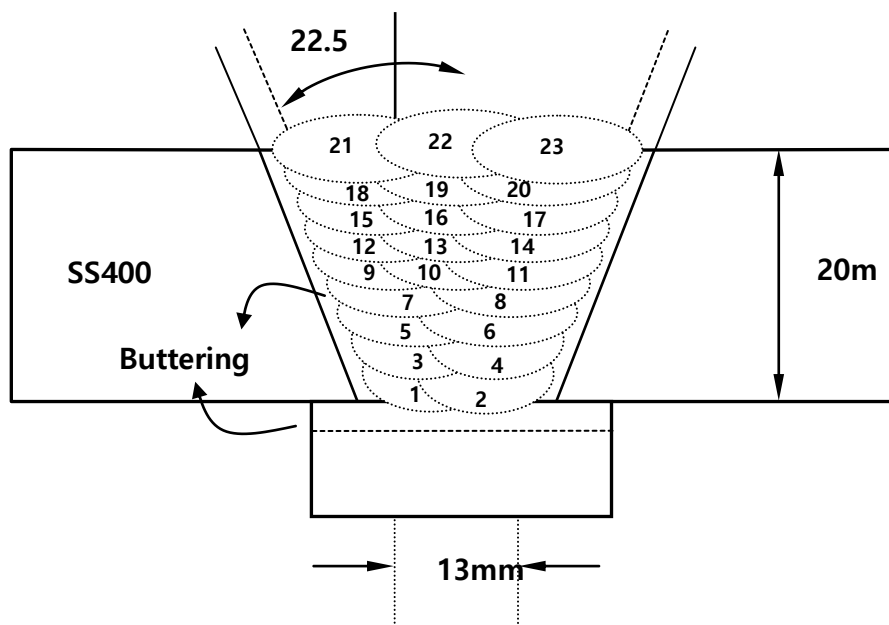


Figure 1. Schematic diagram of the weld metal

Table 1. Welding condition of specimen

Filler Metal	Current Range(A)	Voltage Range(V)	Welding Speed (mm/min)	Interpass Temp.	Heat Input (J/mm)
Inconel 625	130~140(DC+)	24 ~ 26	150~180	Max. 150°C	1.04~1.46

Table 2. Composition of specimen (wt%)

	C	Mn	Fe	P	S	Si	Cu	Ni	Co(1)	Cr	Nb (+Ta)	Mo
No.1	0.038	0.44	0.98	0.002	0.004	0.15	0.03	64.9	0.02	21.4	2.24	9.64
No.2	0.046	0.47	2.10	0.004	0.001	0.16	0.06	62.2	0.02	22.2	3.25	9.10
No.3	0.038	0.44	2.21	0.010	0.003	0.18	0.05	62.7	0.02	20.8	4.26	9.12

2.2. Weld observation

To observe the weld microstructure, the surfaces of welds were ground and polished to the order of 3 μm and 1 μm with #400-#1200 abrasive papers. Afterwards, they were etched with consisting of hydrochloric acid (HCl): nitric acid (HNO<sub>3</sub>) in a ratio of 3:1 [6]. Microstructures of the specimens were observed by optical microscopy, scanning electron microscopy/energy dispersive X-ray spectroscopy(SEM/EDS).

### 2.3. Hardness test

The hardness test was carried out using a Micro Vickers Hardness Tester (Vickers Hardness Tester: FV-700) at a load of 1 kgf and dwell time of 5 s. The hardness was measured at 1 mm intervals over a total range of 20 mm, 10 mm each from the left and right sides according to the Fusion Line of Buttering welding.

### 2.4. Phase analysis

Prior to Electron Back Scattering Diffraction (EBSD) mapping, an X-Ray Diffractometer (Rigaku.D/Max-2A) was utilized to analyze the phases of each weld specimen. The conditions for measurement were set at Cu-K $\alpha$ 1, 2 $\theta$  range of 20°-100° and scan rate of 2 °/min. EBSD mapping was carried out to compare the grain size of each specimen based on its Nb content. Simultaneously, the results were compared using Image Quality (IQ) map and Inverse Pole Figure (IPF) map to analyze the growth tendencies of the phases in each specimen. The  $\gamma$ -NiCr phase was used for the phase information during mapping. The magnification was 50 $\times$  and the step size was 2.5  $\mu\text{m}$ . OIM Collection7 program from TSL was employed for EBSD data analysis.

### 2.5. Pitting Corrosion Resistance Test

Potentiodynamic polarization test, a kind of electrochemical test, was performed to determine the pitting corrosion resistance of each specimen. After 1  $\mu\text{m}$  polishing, the three specimens (area > 1 cm<sup>2</sup>) were cleaned for testing. The test was carried out using a VersaSTAT 3 (Potentiostat Galvanostat, Princeton Applied Research) and the K0235 Flat Cell was used for the corrosion test. Ag/AgCl/KCl (Saturated) electrode and a platinum foil were used as the reference and counter electrode, respectively. To observe the corrosion behavior of the Inconel alloy in a seawater environment, the polarization experiment was performed in 3.5% NaCl aqueous solution. The detailed conditions of the corrosion test are provided in Table 3.

**Table 3.** Test condition of potentiodynamic polarization test

Electrolyte	Temperature	Initial potential	Final potential	Scan rate
3.5% NaCl	25°C	-0.5V	1.5V	1mV/sec

### 2.6. Intergranular corrosion resistance test

Double Loop-Electrochemical Potentiokinetic Reactivation test (DL-EPR) was conducted based on the International Standard, ISO12732 to investigate the intergranular corrosion resistance [17]. The same equipment from the previous potentiodynamic polarization test was used. The open

circuit potential(OCP) was maintained for 20 min to generate a stable passive film on the specimen surface before the experiment. One liter of aqueous solution for this experiment was made from 146 mL sulfuric acid ( $H_2SO_4$ ) and 238 ml hydrochloric acid (HCl) to which was added 0.001 M potassium thiocyanate (KSCN) [16]. Details of the test condition are given in Table 4. In the present study, the degree of sensitization was determined from the ratio ( $I_r/I_a$ ) of the maximum anode current density ( $I_r$ ) indicated during potential drop and the maximum anode current density ( $I_a$ ) indicated during potential rising.

**Table 4.** Test condition of DL-EPR test

Electrolyte	Temperature	Initial potential	Final potential	Vertex Potential	Scan rate
146ml $H_2SO_4$ + 238ml HCl + 0.001M KSCN	25°C	-1V	-1V	0.9V	1mV/sec

### 3. RESULTS AND DISCUSSION

#### 3.1 Microstructure

Fig. 2 shows the surface SEM images of the three specimens with different Nb compositions. The microstructure showed the typical microstructure of the cast metal[30]. The bright areas in the images indicate subgrain boundaries containing Nb carbide, while the dark areas indicate columnar dendrites [19]. The columnar dendrite structure was mainly observed at a slow cooling rate [20]. Previous studies have reported that Mo plays a role in slowing the cooling rate because of its high thermal conductivity and since it increases the solid solubility of Nb at subgrain boundaries, facilitating columnar dendrite growth [21,22]. It is apparent from the comparison of the three specimens' images that the columnar dendrite structure was mostly found in specimen No.1 since it had the highest Mo content.

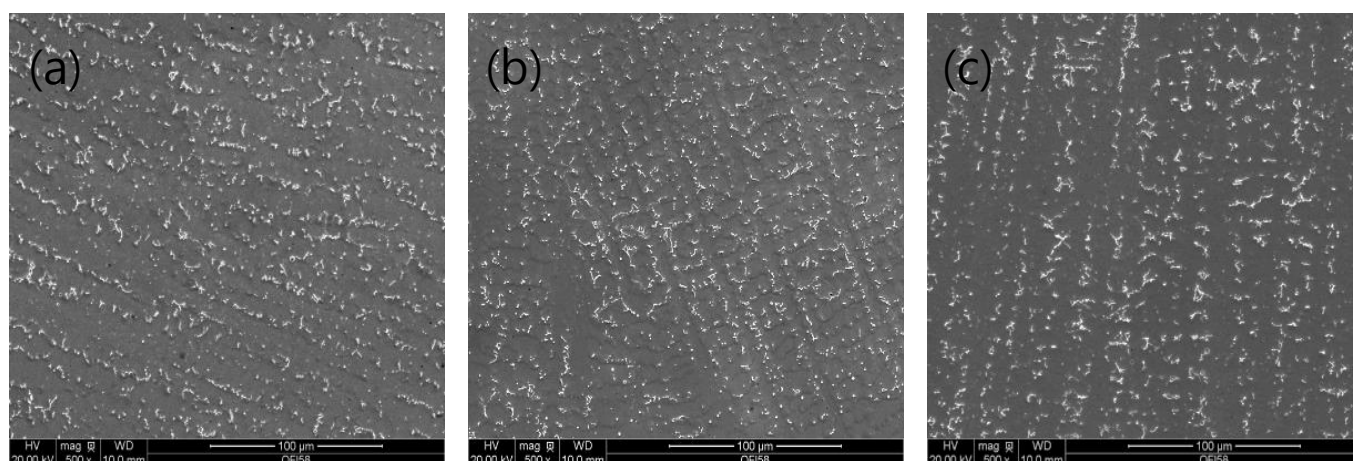


**Figure 2.** SEM image of welds (a) No.1 specimen (b) No.2 specimen (c) No.3 specimen

Fig. 3 shows the EDS image and analysis of the weld. The composition changes in the dendritic nucleus and matrix measured by EDS confirmed a large amount of Nb and Ti in the nucleus. Thus, solidification progressed to the dendritic phase after the precipitation of MC-type intermetallic compounds of Nb and Ti having high melting points[30].

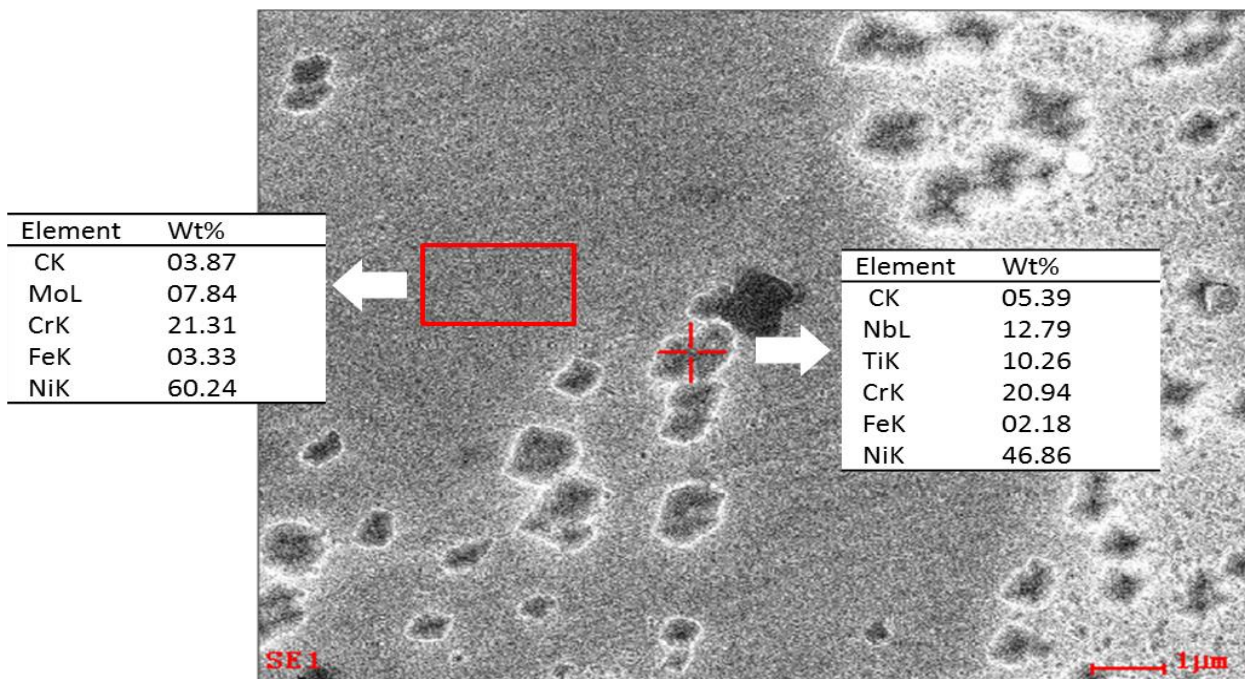


Figure 3. EDS result of dendrite analysis

3.2 Hardness test

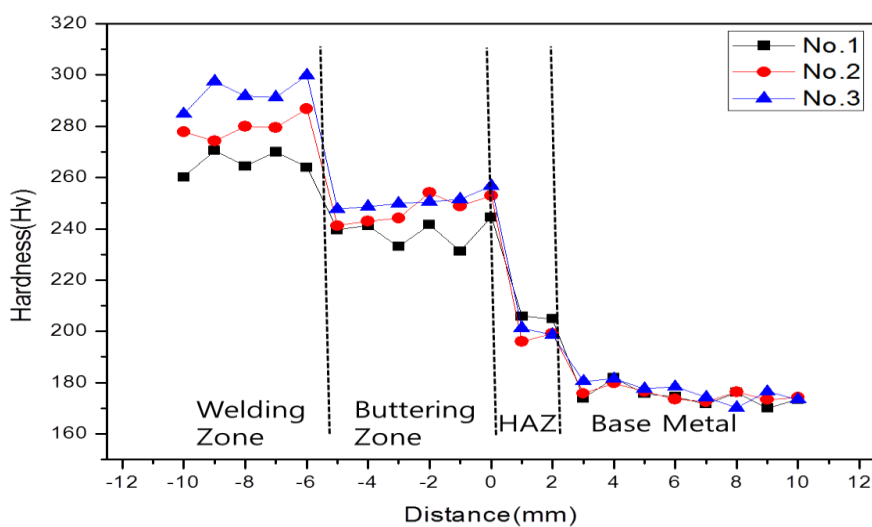
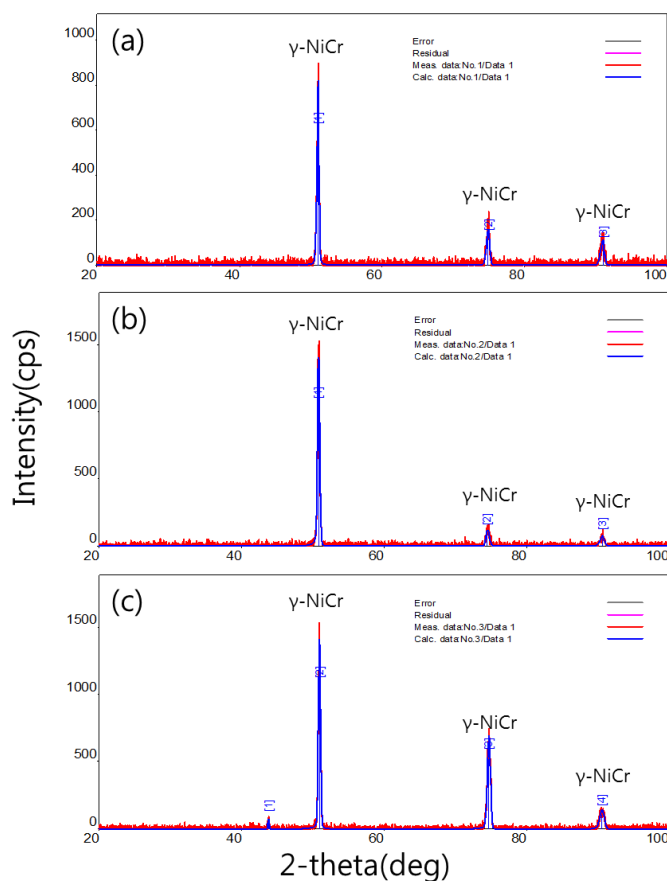


Figure 4. Vickers Hardness value of weldments

Fig. 4 shows the graph comparing the hardness of each specimen. As shown in the graph, a similar hardness value was found in the base metal, HAZ, and the buttering zone. This was because all specimens were processed under the same welding conditions. On the other hand, a significant difference in hardness value could be observed in the welding zone. The No1 specimen exhibited the lowest value, while the No.3 specimen showed the highest value. The effect of hard elements such as Nb and Mo contained in the precipitates at the subgrain boundary was less for the No1 specimen than the other specimens due to the more developed columnar dendrites than subgrain boundaries.

### 3.3 Phase analysis



**Figure 5.** Phase analysis of specimen using X-ray Diffraction (a) No.1 specimen (b) No.2 specimen (c) No.3 specimen

Fig. 5 shows the XRD analysis results of each specimen. Only the  $\gamma$ -NiCr peak could be observed in all three specimens. In general, the peak exhibited the highest intensity for the (111) plane and general patterns were found in all specimens. The peak of the  $\gamma''$  phase or  $\delta$  phase and the NbC carbides could not be observed through XRD analysis since it was difficult to generate secondary phases due to the rapid cooling rate during welding and the fine carbide with size of a few  $\mu\text{m}$  is widely distributed at subgrain boundaries [23].

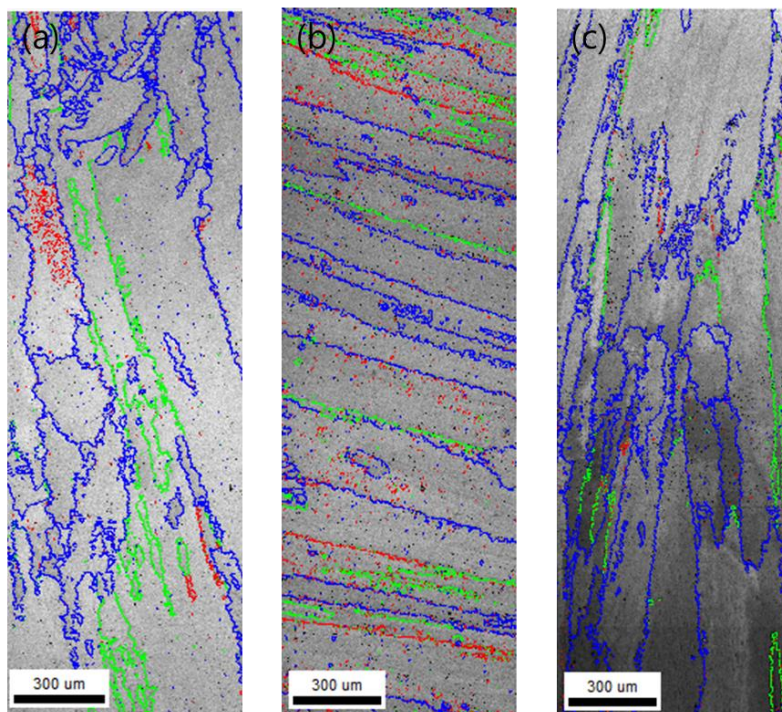


**Figure 6.** Image Quality map of specimen (a) No.1 specimen (b) No.2 specimen (c) No.3 specimen

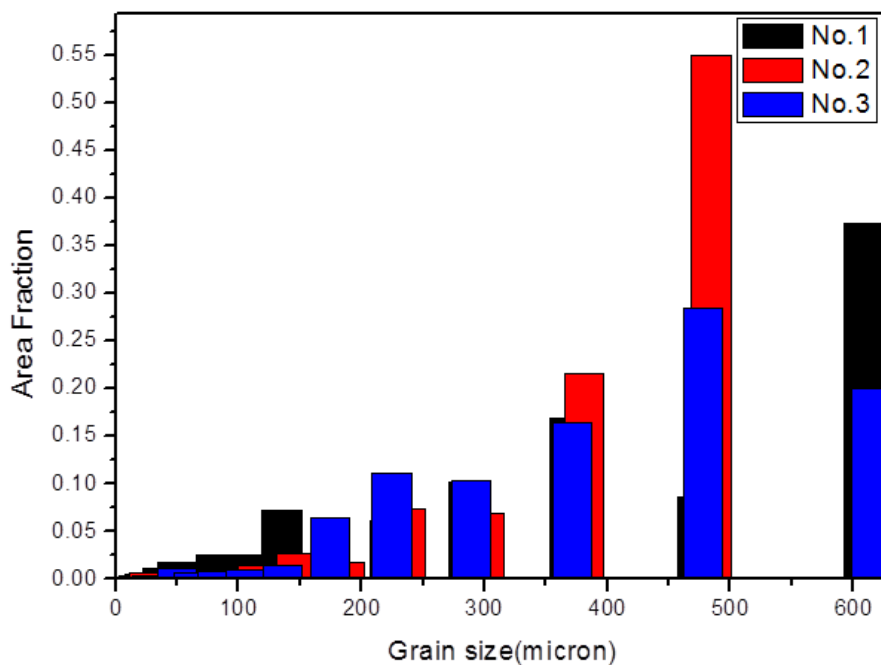


**Figure 7.** EBSD Grain size analysis of specimen

Typically, the secondary phase was formed when the temperature was maintained at more than 600 °C for a certain period of time. Phase data for EBSD analysis was constructed based on the measured XRD data and the EBSD analysis was carried out to measure the grain size. Fig. 6 shows the

IQ map of the specimens analyzed by EBSD. The boundary was mapped with a blue mark for rotation angles more than  $15^\circ$ , green mark for the range  $5^\circ\sim 15^\circ$ , and red mark for the range  $2^\circ\sim 5^\circ$ . Fig. 7 shows the comparison of the measured grain sizes. The x-axis indicates the grain size and the y-axis indicates the fraction at each grain size. The black bar in Fig. 7 refers to the grain size for the No.1 specimen, the red bar for the No.2 specimen, and the blue bar for the No.3 specimen. As can be seen from the graph, a region with the largest grain size of about  $600\ \mu\text{m}$  could be found in No.1. This finding was consistent with the result shown in Fig. 6, confirming the large grain size in the No.1 specimen. As previously mentioned, it was considered that fewer Nb precipitates were formed at subgrain boundaries due to the low Nb content and its role as a nucleus was inferior to the other specimens.

### 3.4 Pitting Corrosion Resistance Test

The potentiodynamic polarization test was carried out at  $25\ ^\circ\text{C}$  in 3.5% NaCl aqueous solution to determine the pitting corrosion resistance of the Inconel 625 weld as a function of Nb content in seawater. The results are presented in Fig. 8. The corrosion potential ( $E_{\text{corr}}$ ), pitting potential ( $E_{\text{pit}}$ ), passive region ( $\Delta E$ ), and corrosion current ( $I_{\text{corr}}$ ) were measured by Tafel extrapolation. The results are shown in Table 5. The corrosion potential and pitting potential of the No.1 specimen were the lowest. However, the overall trends, including the passive region, did not show any significant differences. The study by Lee and Park revealed that increase in pitting potential depends on the Cr content [18,29]. In this study, there was almost no difference in pitting potential between the three specimens due to their similar Cr contents.

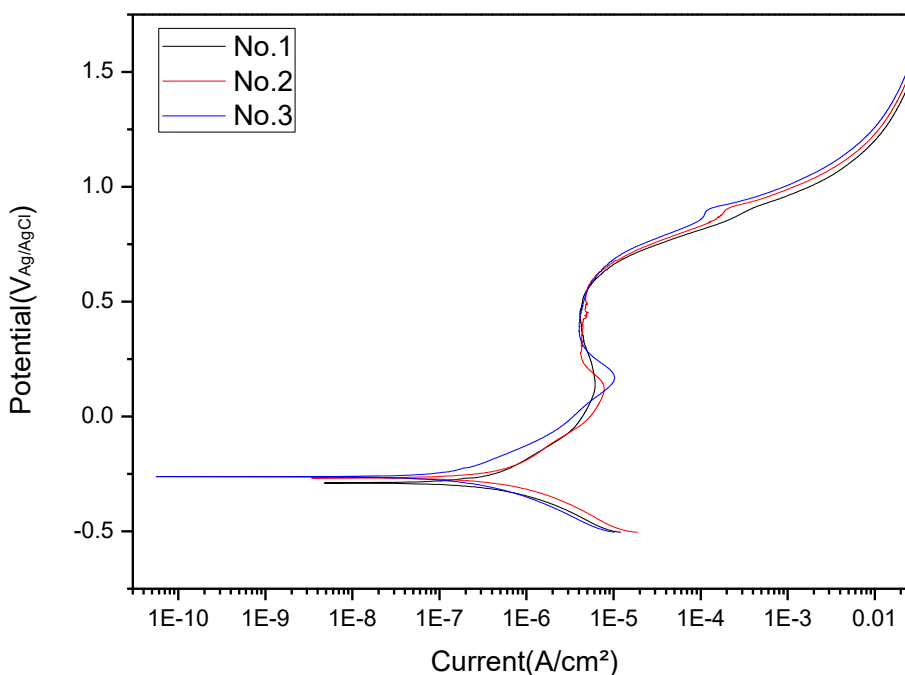


**Figure 8.** The experimental result of potentiodynamic polarization tests

**Table 5.** Corrosion parameters of the potentiodynamic polarization tests in 3.5% NaCl solution

	No.1	No.2	No.3
E <sub>corr</sub>	-288.4mV	-266.9mV	-260.9mV
E <sub>pit</sub>	513.1mV	554.2mV	559.1mV
ΔE	801.5mV	821.1mV	820.1mV
I <sub>corr</sub>	592.3nA	814.6nA	256.9nA

### 3.5 Intergranular Corrosion Test

To evaluate the sensitization degree of intergranular corrosion for Inconel 625 as a function of Nb content, the DL-EPR test was performed at 25 °C using an aqueous solution containing 146 ml sulfuric acid (H<sub>2</sub>SO<sub>4</sub>), 238 ml hydrochloric acid (HCl), and 0.001 M potassium thiocyanate (KSCN). Fig. 9 shows the results from the DL-EPR test.

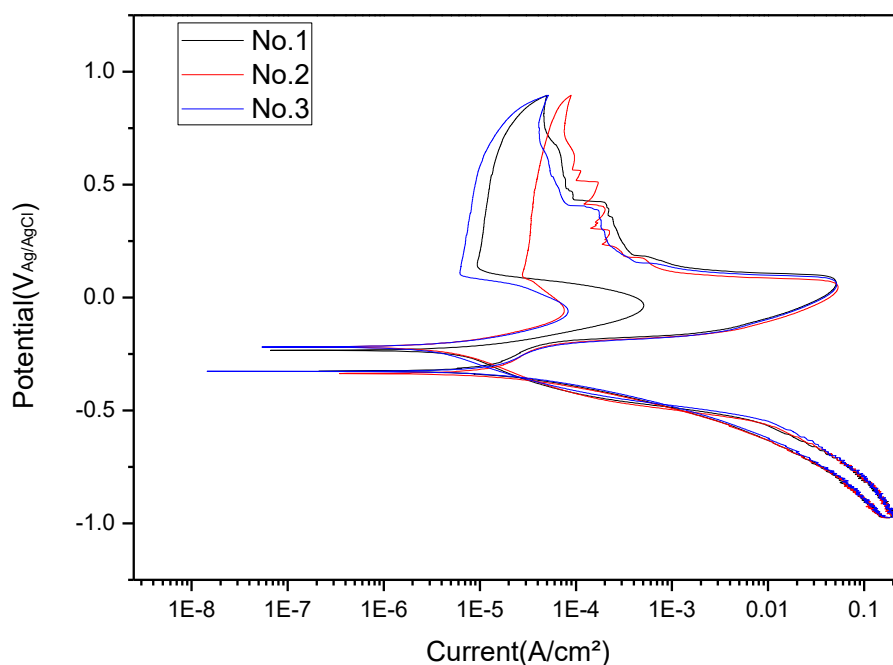


**Figure 9.** The experimental result of DL-EPR tests

The maximum anode current density (I<sub>a</sub>) of the ascending curve, the maximum anode current density (I<sub>r</sub>) of the descending curve, and the ratio of the maximum anode current density (I<sub>r</sub>/I<sub>a</sub>)—which refers to the degree of sensitivity—are presented in Table 6. The narrower the range of I<sub>a</sub> and I<sub>r</sub>

values, the higher the sensitization of intergranular corrosion [16]. The maximum anode current density in the anode curve was similar for the three specimens while the maximum anode current density in the reserve curve was highest in the No.1 specimen. According to the ratio of the  $I_a$  and  $I_r$  values, the sensitivity was found to be 0.0099 for No.1, 0.0014 for No.2, and 0.0016 for No.3. The No.2 and No.3 specimens exhibited a similar degree of sensitization, while the No.1 specimen was confirmed to have a higher degree of sensitization than the other specimens. The degree of sensitization is highly correlated with the depletion region of Cr and Mo [24,25]. In this case, the small amount of Nb did not sufficiently react with C, leading to Cr-carbide ( $M_{23}C_6$ ) formation in the solidification process and the larger Cr depletion region compared to the other specimens. The No.1 specimen contains 2% Nb, which is lower than the typical Nb content of Inconel 625 (3.15~4.15 wt%). Since the carbon did not sufficiently react to form NbC at the subgrain boundary, the depletion zone of Cr increased resulting in higher sensitivity to intergranular corrosion.

**Table 6.** Degree of sensitization

	$I_a$	$I_r$	$I_r/I_a$
No.1	50.9mA	505 $\mu$ A	0.0099
No.2	52.5mA	75.4 $\mu$ A	0.0014
No.3	50.5mA	81.8 $\mu$ A	0.0016

#### 4. CONCLUSIONS

Three specimens with different Nb contents were produced by the SMAW technique after buttering on carbon steel. The microstructure was observed and the corrosion behavior was analyzed through electrochemical tests.

1) The microstructure observation results confirmed the columnar dendrite was the most developed in the No.1 specimen (having the lowest Nb content).

2) The hardness test revealed that the hardness value of the welds increased with increasing Nb content.

3) The phase analysis results by EBSD showed the largest grain size for No.1 specimen (having the lowest Nb content).

4) The potentiodynamic polarization test was done in seawater conditions on three specimens with different Nb contents using a 3.5% NaCl aqueous solution. Overall, the corrosion potential, pitting potential, and passive region values were similar.

5) The DL-EPR test was performed using an aqueous solution containing 146 ml  $H_2SO_4$  + 238 ml HCl + 0.001 M KSCN to determine intergranular corrosion. The  $I_r/I_a$  value, which determines the

degree of sensitization, was found to be similar for the No.2 and No.3 specimens, while the No.1 specimen exhibited a value about 7 times higher.

6) The No.1 specimen having low Nb content could not have sufficient reaction with C at the subgrain boundaries, resulting in an increase in the depletion region of Cr. Thus, it was considered to be more sensitive to intergranular corrosion.

#### ACKNOWLEDGEMENTS

This investigation was supported by the Dong-A University Research Fund

#### References

1. W.F. Smith, Structure and Properties of Engineering Alloy, McGraw-Hill, (1981) U.S.A..
2. Corrosion of Nickel Base Alloys, ASM International, Metals Handbook, 9th Ed., (1987) U.S.A..
3. V. Shankar, K. B. S. Rao and S. L. Mannan, *Journal of Nuclear Materials*, 288 (2001) 222.
4. P. Ganesan, C. M. Renteria and J. R. Crum, *Superalloys*, 718 (1991) 625.
5. L. Ferrer, B. Pieraggi and J. F. Uginet, *Superalloys*, 718-625 (1991) 217.
6. C.C. Silva, H. C. de Miranda, M. F. Motta, J. P. Farias, C. R. M. Afonso and A. J. Ramirez, *Journal of Materials Research and Technology*, 2 (2013) 228.
7. M. Rozmus-Górnikowska, M., Ł. Cieniek, M. Blicharski and J. Kusiński, *Archives of Metallurgy and Materials*, 59 (2014) 1081.
8. M. C. Maguire and J. R. Michael, Weldability of alloy 718-625 and variants., Third International Special Emphasis Symposium on Superalloys (1994).
9. F. Cortial, J. M. Corrieu and C. Vernot-Loier, *Metallurgical and Materials Transactions A*, 26 (1995) 1273.
10. M. J. Cieslak, T. J. Headley, A. D. Romig and T. Kollie, *Metallurgical Transactions A*, 19 (1988) 2319.
11. J. W. Yu, S. H. Park, C. S. Kim and C. Y. Kang, *Journal of Welding and Joining*, 30 (2012) 106.
12. J. J. Kai, C. H. Tsai, T. A. Huang and M. N. Liu, *Metallurgical Transactions A*, 20 (1989) 2057.
13. J. C. Lippold, S. D. Kiser and J. N. DuPont, *Welding metallurgy and weldability of nickel-base alloys*, John Wiley & Sons, (2011).
14. J. N. DuPont, *Welding J.*, 10 (1988) 417.
15. H. C. Yoo, *Journal of Welding and Joining*, 31 (2013) 11.
16. M. Prohaska, H. Kanduth, G. Mori, R. Grill and G. Tischer, *Corrosion Science*, 52 (2010) 1582.
17. BS EN ISO12732:2008, Corrosion of metals and alloys-Electrochemical potentiokinetic reactivation measurement using the double loop method(based on Cihal's method), BSI, (2006).
18. J. B. Lee, *Mater. Chem. & Phys.*, 99 (2006) 224.
19. X. Xixue, X. Di and B. Wang, *Journal of Alloys and Compounds*, 593 (2014) 110.
20. T. E. Abioye, D. G. McCartney and A. T. Clare, *Journal of Materials Processing Technology*, 217 (2015) 232.
21. M. M. Tavakkoli and S.M. Abbasi, *Materials & Design*, 46 (2013) 573.
22. G.S. Shin, J.Y. Yun, M. C. Park and S. J. Kim, *Materials Characterization*, 95 (2014) 180.
23. G. P. Dinda, A. K. Dasgupta and J. Mazumder, *Materials Science and Engineering A*, 509 (2009) 98.
24. J. N. Dupont, *Metallurgical and Materials Transactions A*, 27 (1996) 3612.
25. R. M. Deacon, J. N Dupont and A. R Marder, *Materials Science and Engineering A*, 460 (2007) 392.

26. H. S. Lim, T. H. Kim and K. C. Park, *Journal of Welding and Joining*, 21 (2003) 172.
27. I. Varol, W. A. Baeslack and J.C. Lippold, *Metallurgy.*, 23 (1989) 1.
28. C.H. Shek, G. J Shen, J.K.L. Lai and B.J. Duggan, *Mater. Sci. Technol.*, 10 (1994) 306.
29. I.C. Park and S.J. Kim, *J. Korean Inst. Surf. Eng.*, 49 (2016) 172.
30. P. Petrzak, K. Kowalski and M. Blicharski, *Acta Physica Polonica, A*, 130 (2016) 1041.

© 2018 The Authors. Published by ESG ([www.electrochemsci.org](http://www.electrochemsci.org)). This article is an open access article distributed under the terms and conditions of the Creative Commons Attribution license (<http://creativecommons.org/licenses/by/4.0/>).